# Experimental and Simulative Study on IM-DD Transmission and Large Chirped-Pulse DAS Coexistence

*Original*
Experimental and Simulative Study on IM-DD Transmission and Large Chirped-Pulse DAS Coexistence / Pellegrini, S., Hernandéz-Martin, L., Brusin, A.M.R., Rizzelli, G., Ania-Castañon, J.D., Bosco, G., Gaudino, R., Martins, H.F.. - In: JOURNAL OF LIGHTWAVE TECHNOLOGY. - ISSN 0733-8724. - 44:5(2026), pp. 1743-1753. [10.1109/jlt.2025.3644664]

*Publisher:*
IEEE

*Published*
DOI:10.1109/jlt.2025.3644664

# Experimental and Simulative Study on IM-DD Transmission and Large Chirped-Pulse DAS Coexistence

Saverio Pellegrini, Laura Hernandéz-Martin, Ann M. Rosa Brusin, Giuseppe Rizzelli, Juan Diego Ania-Castañon, Gabriella Bosco, *Member, IEEE*, Roberto Gaudino, *Senior Member, IEEE*, and Hugo F. Martins

***Abstract*—Distributed acoustic sensing (DAS), implemented through phase-sensitive optical time-domain reflectometry ($\phi$OTDR), has gained attention in geophysical and telecommunications environments. By utilizing the existing telecom infrastructure, DAS facilitates self-monitoring of networks and external events observation, from human activities to large-scale geophysical phenomena. However, integrating it with data signals on the same fiber is challenging, as DAS employs higher power signals that can interact with data channels.**

**Although increasing DAS performance with higher bandwidths is possible, practical applications have mostly been limited to 1 GHz due to cost and complexity constraints. This paper investigates the coexistence conditions of DAS, specifically direct detection (DD) chirped-pulse-$\phi$OTDR (CP-$\phi$OTDR), with intensity-modulated and DD (IM-DD) telecommunication systems, both operating at comparable complexities (5 GHz chirp and 10 Gbit/s), particularly interesting for metro/access contexts. We varied the frequency spacing of data and DAS channels, the DAS pulse peak power, and the receiver optical filter bandwidth, identifying the conditions for feasible coexistence.**

**Our analysis shows that nonlinear Kerr-induced modulation instability (MI) is the main impairment affecting IM-DD channels co-propagating with DAS. In this scenario, MI cannot be approximated as originating from a single frequency source, and the observed nonlinear impairments vary along the pulse with its sweeping central frequency. Numerical simulations validate the experimental results, showing close alignment.**

***Index Terms*—Fiber sensing, distributed acoustic sensing, chirped-pulse, IM-DD, data transmission and sensing coexistence**

## I. INTRODUCTION

THE dense telecommunication-driven installation of optical fibers in both terrestrial and submarine environments has sparked interest in exploiting the same network infrastructure as a distributed sensor for detecting events occurring around fiber cables. These events can range from fiber cuts due to maintenance works, to malicious intrusions in central offices or street cabinets, to serious hazards that pose significant risk to lives and infrastructure, such as earthquakes and tsunamis, and should be actively detected and monitored to provide timely warnings.

Using the vocabulary that is currently under standardization as an ITU-T initiative, titled DFOS (distributed fiber optic sensing) and described in [1], two options are made available to integrate sensing capabilities over telecom systems:

- **Backscattering-based sensing.** This is typically implemented through distributed acoustic sensing (DAS) interrogators, added to the traditional optical transmission hardware.
- **Feed-forward (FF) sensing.** This option utilizes the received data signal to extract sensing information. The most common FF solution is based on the analysis of received state of polarization (SOP) [2], but phase-based [3], [4] or interferometric-based [5] FF solutions have also been proposed.

The two groups of solutions have pros and cons. FF solutions require minimal extra hardware (or in some cases no new hardware at all [3], [6], [7]) but have limited or no event localization capabilities [8], [9]. DAS solutions are much more expensive (in terms of both CAPEX and OPEX) but enable accurate positioning.

In this paper, we focus on the coexistence of standard data transmission and DAS on the same fiber. As mentioned above, DAS technology, typically based on phase-sensitive optical time domain reflectometry ($\phi$OTDR) [10], [11], has already proven to be effective in accurately localizing axial strain in various scenarios [12]–[14]. As a result, it achieved significant commercial success in important niche applications, such as monitoring oil and gas pipelines, and is increasingly being recognized in geophysical applications. The basic working principle of DAS systems is to transmit high-peak-power pulses at a fixed repetition rate while measuring the backscattered traces, enabling the localization of strain by evaluating the time-of-flight towards the transmitter. The DAS pulse peak power and the repetition rate fix the sensing range of the system, usually around a few tens of km, while the pulse duration fixes the spatial resolution.

DAS can operate with coherent or direct detection (DD), similarly to telecommunication systems. With coherent detection, perturbations can be tracked by monitoring the phase variation of the Rayleigh backscattered signal. By recovering the complex optical field, matched filtering (MF) can be applied, allowing for long modulated signals (instead of short pulses) to be sent into the fiber and recovering the

Saverio Pellegrini, Ann M. Rosa Brusin, Gabriella Bosco, and Roberto Gaudino are with the Department of Electronics and Telecommunications, Politecnico di Torino, 10129 Torino, Italy (e-mail: saverio.pellegrini@polito.it).

Giuseppe Rizzelli is with the Photonext Center, Politecnico di Torino, 10129 Torino, Italy.

Laura Hernandéz-Martin, Juan Diego Ania-Castañon and Hugo F. Martins are with the Instituto de Optica “Daza de Valdés”, CSIC, 28006 Madrid, Spain.

This work was partially supported by the SURENET project, funded by the European Union – Next Generation EU within the PRIN 2022 program (D.D. 104 - 02/02/2022 Ministero dell’Università e della Ricerca). The manuscript reflects only the authors’ views and opinions and the Ministry cannot be considered responsible for them. This work was supported in part by the MCIN/AEI/10.13039/501100011033 and European Union “NextGenerationEU”/PRTR under grants PID2021-128000OB, PRE2022-104176, RYC2021-035009-I, CNS2022-135925, CPP2022-009772, PID2024-162301OA-C22, CPP2024-011822, PID2024-160056OB-C21.

impulse response in post-processing. Such an operation provides flexibility in system parameters, enabling both long-range operation (beyond $100$ km [15]–[17]) and improved spatial resolution [18], [19]. Long haul operation using MF and optical repeaters compatible with the telecom infrastructure, has also been recently pursued, demonstrating operation over $1000$ km [20], [21]. For coherent detection, the use of ultra narrow-linewidth lasers is a mandatory system requirement, as the phases of the backscattered traces need to be coherent, being unfortunately one of the main reasons for the DAS's high CAPEX cost.

On the other hand, using DD, single-shot linear measurement DAS systems are also possible with the use of chirped-pulse $\phi$OTDR (CP-$\phi$OTDR) [22]. CP-$\phi$OTDR presents fundamentally different trade-offs than traditional phase-measuring DAS, excelling in large strain detection [23], [24], and long-term ($> 24$ hours) operation [25]–[27]. While operation in up to $100$ km has been demonstrated [28], the highest performances are traditionally reported at shorter distances (typically at up to $\sim 50$ km). The complexity is also reduced, given the simpler DD scheme used (single DD photodetector/digitizer), and the fact that laser stability requirements can be relaxed by 1-2 orders of magnitude (e.g., operating with $1$ MHz laser linewidths [29]). This makes DD CP-$\phi$OTDR an ideal candidate for low cost monitoring of access/metropolitan links. We remark that CP-$\phi$OTDR has been widely used in the last decade and is a commercially available technology. The interested reader is invited to read the extended review of the technique, available in [28], where the finer details, advantages, and trade-offs of the technique are analyzed in depth.

Note that the DAS and telecommunication data compatibility requirements are also fundamentally different between the two operations: with coherent detection DAS and use of MF, a lower peak power can be used, but overlapping during a higher percentage of time (duty cycle can in fact be close to 1 [30]). With DD DAS, higher peak power is used, but overlapping during shorter periods (duty cycles typically of $10^{-3}$-$10^{-4}$ [31]). Recent research on the coexistence of DAS and telecommunication systems [1], [20], [31] has shown that high-peak-power pulses can induce Kerr effects on data wavelengths, achieving coexistence under specific conditions that depend significantly on the system configurations.

Regarding the used optical bandwidth, whilst in telecommunications the use of tens of GHz has become standard use, so far, DAS operation (both academic and commercial) has been mostly limited to operations below $1$ GHz (due to an increase in cost/complexity which does not match the traditional DAS applications). In this regime, pulses can essentially be approximated as a single frequency signal when studying nonlinearities arising in DAS [32] and coexistence [31]. However, fundamentally, telecommunications and DAS can operate at similar bandwidths, and an increase in optical bandwidth is known to allow for an increase in DAS performance. As an example, using DD CP-$\phi$OTDR with $8$ GHz optical chirp, the measurable single-shot strain variation was increased to $\pm 3\mu\varepsilon$ (two orders of magnitude higher than traditional phase-measurement DAS for the same spatial resolution) at kHz operation [24]; and long-term ($> 24$ hours) high sensitivity (n$\varepsilon$ [24], $\mathrm{mK}$ [27]) measurements were demonstrated. In this regime, with optical bandwidths of 10 GHz that can no longer be approximated as a single central frequency pulse, the impact of nonlinearities in DAS has only recently been described in detail [27], and, to the best of our knowledge, no co-existence studies have yet been performed.

In this paper, we will focus specifically on the coexistence between large chirped-pulse DAS and intensity-modulated and direct detection (IM-DD) data transmission on the same fiber, both operating at similar optical bandwidths ($5$ GHz optical chirp, $10$ Gbit/s), and both envisaged for DD operation over a few tens of km. The possible scenario of application is the one analyzed in [1]: metropolitan single span, inter-data center or access networks, which are still largely based on legacy IM-DD transceivers. In these scenarios, typically covering a few tens of km, CP-$\phi$OTDR can give excellent sensing and localization capabilities. Moreover, the ITU-T DFOS initiative [1] discussed above is pushing for incorporating the sensing signal into the ITU-T grid in access or metro DWDM legacy systems [33], highlighting the growing interest in this topic.

This work extends our previous conference paper [34], where we presented initial results focused on dense frequency spacings of 50 GHz and 100 GHz between co-propagating data and sensing channels. In this paper, we investigate the frequency spacings up to $400$ GHz, varying the DAS peak power, and adjusting the receiver optical filter bandwidth, as outlined in Section II. We also emphasize in Section III the physical interpretation of the propagation effects on the data signal, analyzed for both co-propagation and counter-propagation. A major addition is the confirmation of our findings through detailed time-domain split-step simulations, in Section IV, which suggest system-level solutions for enhancing coexistence. Section V concludes the paper with final discussions.

## II. EXPERIMENTAL SETUP

In this section, we describe the experimental setup illustrated in Fig. 1a), which we used to investigate the coexistence of large chirped-pulse DAS and telecommunication IM-DD systems.

On the DAS side, we experimentally implemented the chirped pulse generator only, without analyzing the reception of the backscattered traces (it was, anyway, shown in [31], [35] that data impact on DAS performance is minimal, provided that appropriate optical filters are used). The DAS chirped pulses are generated employing a narrow-linewidth ($\sim$100 Hz) ultra-stable laser (referred to as "DAS laser" in Fig. 1a)), with central wavelength $\lambda_0 = 1550$ nm ($f_{DAS} = 193.414$ THz), which is then modulated using an I/Q Mach-Zehnder modulator (MZM), driven on its two electrical arms by an arbitrary waveform generator (AWG). The pulse intensity was shaped as a 4th order Super-Gaussian, with full-width-half-maximum (FWHM) duration $\tau = 80$ ns. Proper sinusoidal signals, Super-Gaussian-shaped, generate the optical chirp inside the pulse, which ranges from starting frequency $\nu_0 = -1$ GHz to final frequency $\nu_f = -6$ GHz, thus with bandwidth $\Delta\nu = 5$ GHz.

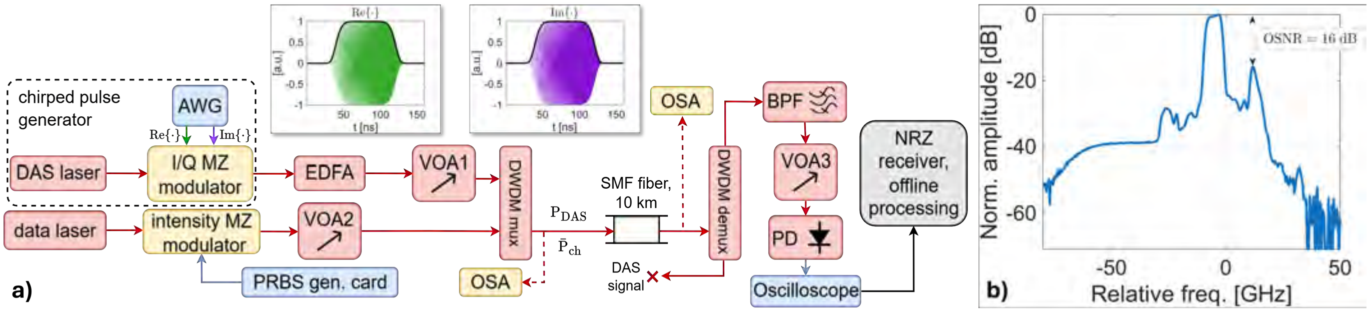

Fig. 1. a) Experimental setup used for the coexistence analysis of the DAS pulse with data channels propagating in a 10 km SSMF. The inset shows the real (green) and imaginary (purple) parts of the complex chirp, driving the I/Q MZ. The black line is the Super-Gaussian intensity envelope. b) Transmitted spectrum of the large chirped-pulse DAS alone, normalized to its maximum.

The inset of Fig. 1a) shows the (ideal) real and imaginary parts of the generated chirped pulse, and its Super-Gaussian intensity envelope (black continuous line). The electrical signals sent to the AWG were also pre-distorted to compensate for the driver and the limitations of the MZM electrical frequency responses, resulting in less than 1 decibel (dB) variation from $\nu_0$ to $\nu_f$ amplitude. The DAS signal was sent once every $\sim$ 3.2 $\mu$s, to match the data pseudo-random bit sequence (PRBS) periodicity, as detailed further on, corresponding to a DAS duty cycle of $\sim 2.4\%$. Commercial DAS duty cycles are much smaller, but our choice was motivated by the need to simplify the experimental signals post-processing (i.e., by using shorter signal acquisition windows) and by the fact that, as mentioned above, we are not evaluating the DAS sensing-related performance, but only its impact on data channels. After its generation, the DAS pulse was amplified by an erbium doped fiber amplifier (EDFA), its peak power $P_{DAS}$ regulated by a variable optical attenuator (VOA1 in Fig. 1a)) and measured right before fiber propagation. The DAS peak powers used for this study varied between $\sim$ 20 dBm to $\sim$ 29 dBm, as it is the most commonly used power range for short-metro fibers. Note that, for SMF fibers (with effective lengths of $\sim$ 20 km), pulse peak powers are capped due to the effects of MI at $\sim$ 23 dBm [28], [32]. However, for shorter fibers, peak powers can be increased in inverse proportion to the fiber's length (e.g., $\geq$ 30 dBm for 5 km fibers, [36]). It should be noted that for the particular case of CP-$\phi$OTDR technology, a lower signal-to-noise-ratio variability with peak power is expected than in phase-measuring DAS, as long as the trace visibility is maintained (i.e, nonlinear effects are avoided) and enough signal-to-noise-ratio is available to avoid large errors [37]. To ease readability, in the remainder of the paper, the optical spectra will always be plotted with respect to a relative frequency axis where conventionally 0 GHz corresponds to the DAS laser central optical frequency $f_{DAS}$.

On the telecommunication side, the IM-DD non-return-to-zero (NRZ, PAM-2) data transmission was generated using a commercial PRBS generator card, set at 10 Gbit/s and using a PRBS sequence with $2^{15} - 1$ bits period, resulting in a periodicity of $T_{PRBS} \sim 3.2$ $\mu$s. This signal electrically drives an intensity MZM, optically fed by a tunable distributed feedback (DFB) laser, referred to as "data laser" in Fig. 1a). The average data signal is set by means of VOA2 to $\bar{P}_{ch} = -2$ dBm, allowing for acceptable received optical power (ROP), measured right at the fiber input (see Fig. 1a)). A 10 km standard single-mode fiber (SSMF) G.652 was used as the fiber link under test, emulating the short-reach single span scenarios outlined in Section I. Different frequency separation values $\Delta f$ of the data carrier from the DAS central frequency $f_{DAS}$ have been considered: 50 GHz, 100 GHz, 200 GHz, 400 GHz. To this purpose, a dense wavelength division multiplexing multiplexer (DWDM mux) has been used to merge the DAS and data signals into the fiber input, while at the fiber output, a DWDM demultiplexer (DWDM demux) has been used to separate them. The DWDM mux/demux has a pass band of 80 GHz.

Fig. 1b) shows the measured normalized average transmitted optical spectrum of the chirped pulse, measured right before fiber propagation, thus after the DWDM mux. The resolution bandwidth of the optical spectrum analyzer (OSA) was 0.01 nm (1.25 GHz). As mentioned above, 0 GHz refers to the DAS central frequency $f_{DAS}$. The 5 GHz chirp content is visible in Fig. 1b) on the left side (from $\nu_0 = -1$ GHz to $\nu_f = -6$ GHz). For reasons that will become clearer later in the paper, it is useful to comment on the optical noise that is present on this transmitted DAS pulse spectrum. Here we define a transmitted optical-signal-to-noise-ratio (OSNR) as the difference in dB between the pulse spectral peak (arbitrarily normalized to 0 dB in Fig. 1b)) and the (non-flat) surrounding optical noise. We observed two main optical noise sources:

1) *EDFA amplified spontaneous emission (ASE) noise*. This is the relatively flat spectral component, mainly visible around $-50$ GHz in Fig. 1b), and present in the whole DWDM mux 80 GHz band. The related OSNR is about 40 dB. This noise contribution is always active, even outside the DAS pulse occurrence.
2) *I/Q modulator spurious noise effects*. The combination of the AWG electrical signal source and the following I/Q modulator used in our experiments generates some spurious harmonics on either side of the main lobe in Fig. 1b). The strongest harmonic is located at about $+10$ GHz from the DAS center frequency and generates a "local" OSNR of about 16 dB, whereas the other significant harmonic, located at $-25$ GHz, has OSNR =

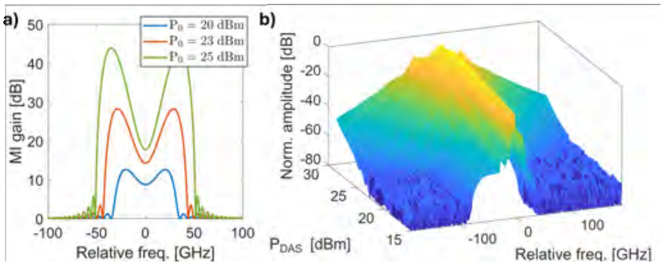

Fig. 2. a) Theoretical MI gain curve [38], [39] generated by a single frequency source, considering $\gamma = 1.3$ W$^{-1}$/km, $\beta_2 = -22$ ps$^2$/km and a 10 km SSMF fiber. b) Received spectra obtained after fiber propagation versus different $P_{DAS}$, when the chirped pulse alone is propagated. The graph is normalized to the maximum value among all the measured spectra.

30 dB. This spurious noise source is only present inside the DAS pulse.

It should be noted that in our experiments, when we vary $P_{DAS}$ through VOA1, the two aforementioned noise contributions, and therefore the OSNR levels, vary accordingly.

After fiber propagation and channels separation through DWDM demux, the modulated data signal is further filtered through an optical bandpass filter (BPF) with the same central frequency as the data channel and bandwidth $B_{\mathrm{rx}}$. The role of this filter is quite important and will be discussed later. Different $B_{\mathrm{rx}}$ values have been tested, specifically $B_{\mathrm{rx}} = 14$ GHz, 20 GHz, 30 GHz, and 50 GHz. The resulting total optical filtering on the data signal at the fiber output, which is given by the cascade of the DWDM demux and the BPF, provides an effective DAS channel suppression of more than 60 dB. This means that any linear optical crosstalk from DAS pulse onto the data signal is excluded.

On the data signal receiver side, we used VOA3 to change the ROP $P_{\mathrm{rx}}$ reaching the photodiode (PD), thus allowing bit error ratio (BER) measurements for different $P_{\mathrm{rx}}$ values. The electrical signal from the PD is then digitized through a real-time oscilloscope (RTO) and processed offline through a standard NRZ DD receiver, computing the BER through the error counting technique. As a benchmark for our experimental analysis, i.e. without DAS signal, we set $P_{\mathrm{rx}} = -20$ dBm to obtain BER$\simeq 10^{-4}$. We will refer to this baseline as $BER_{noDAS}$ for the considerations in the next sections.

## III. EXPERIMENTAL RESULTS

We present here the experimental results, starting with Subsection III-A, which highlights important considerations about the nonlinear propagation of the DAS signal in the fiber, to underline the main effects involved. Subsection III-B shows the resulting impact on the data channel from both spectral and time-domain perspectives. Lastly, Subsection III-C discusses the BER degradation as a function of different system parameters.

### *A. Considerations on nonlinear effects resulting from the propagation of the DAS signal alone*

As it is known from nonlinear optics theory [38], modulation instability (MI), also called parametric gain (PG), is one of the main impairments generated by high-peak-power pulse propagation in optical fibers, responsible for a very peculiar in-band amplification around the central frequency of the pulsed signal. In the context of DAS, it is known to be one of the main effects for high power pulses, typically limiting $P_{DAS}$ to around 23-25 dBm [32] in practical applications. To grasp MI key features, Figure 2a) illustrates the MI gain that a single frequency pulse propagation would generate [39] centered at $f_{DAS}$, showing the strong dependency that the gain and the frequency position of the main lobes have with increasing pulse peak powers $P_0$. Particularly, the angular frequency $\Omega_{max}$ at which the MI gain has its two symmetric maxima (i.e., the lobes positions) is described by Eq. (1)

$$\Omega_{max} = \pm \left( \frac{2\gamma P_0}{|\beta_2|} \right)^{1/2}, \tag{1}$$

where $\gamma$ is the fiber Kerr nonlinear coefficient, and $\beta_2$ the group velocity dispersion constant. In Fig. 2a), the fiber is considered to be 10 km long, with $\gamma = 1.3$ W$^{-1}$/km and $\beta_2 = -22$ ps$^2$/km, typical values for a telecommunication SSMF fiber. Eq. (1) and Fig. 2a) highlight that a higher peak power corresponds to a broader and more intense noise amplification. This may become critical for the coexistence with the telecommunication channels, particularly close to the DAS pulse, as the crosstalk generated by the MI could induce distortions on data. While Fig. 2a) shows the theoretical MI gain, Fig. 2b) shows the spectra as recorded by the OSA, in our experimental setup, after the 10 km fiber and for different $P_{DAS}$ values, when the chirped pulse was transmitted alone. The graph in Fig. 2b) is normalized (as in most of the other spectral curves reported in this paper) to set the maximum to 0 dB. The presence of the MI effect is quite evident, since the received spectra broadens with increasing peak power, and consequently, the in-band noise (due to both I/Q harmonics and ASE) increases. This effect can be observed with a DAS peak power starting at 21 dBm.

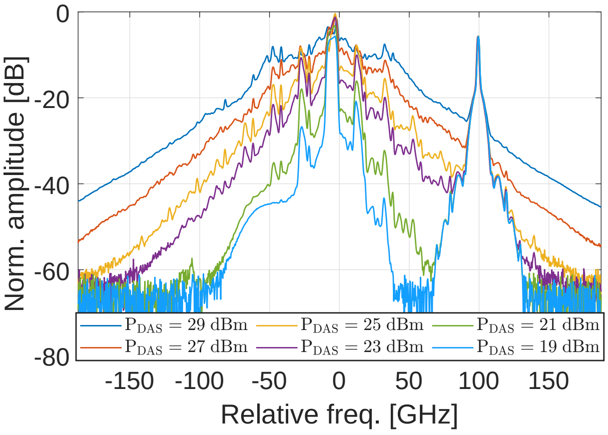

Fig. 3. Average spectra of the co-propagating large chirped-pulse DAS and $\Delta f = 100$ GHz spaced data channel recorded by the OSA right after fiber propagation for different $P_{DAS}$.

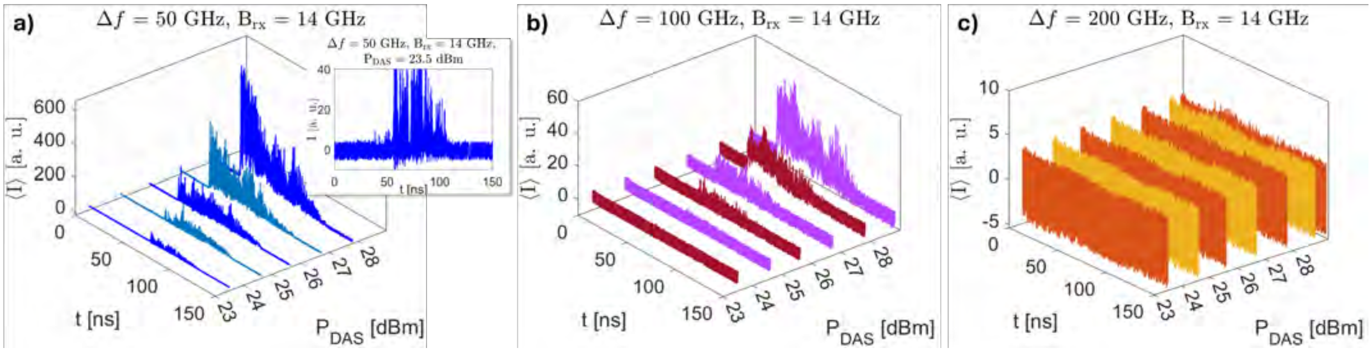

Fig. 4. Data signal average intensity $\langle I \rangle$ evolution along the pulse co-propagation for $B_{\mathrm{rx}} = 14$ GHz when a) $\Delta f = 50$ GHz, b) $\Delta f = 100$ GHz and c) $\Delta f = 200$ GHz, versus $P_{DAS}$. Different colors are only used to provide contrast between lines and enhance readability. Inset in a) represents the non-averaged intensity $I$ evolution for the case with $\Delta f = 50$ GHz, $B_{\mathrm{rx}} = 14$ GHz and $P_{DAS} = 23.5$ dBm.

### B. *Spectral and time domain measurements on data signal*

We will now examine the spectral and time-domain distortions caused by the MI-crosstalk on the data signal, based on experimental results obtained when both DAS and data channels are active. To this purpose, Fig. 3 shows the spectrum of data co-propagated with the DAS signal, recorded at the fiber output before the optical filtering, in the case of $\Delta f = 100$ GHz channel frequency spacing. This figure illustrates how the MI effect on DAS can affect the data signal when the spectral separation is small enough for it to fall within the DAS MI-generated bandwidth. In this case, two detrimental effects take place:

1) the DAS transmitter intrinsic noise (see previous Subsection III-A and Fig. 1b)) is strongly enhanced by MI, thus reducing the OSNR around the data channel;
2) MI (which can also be interpreted as a "local" spectral gain) amplifies the data signal in a complex and non-linear way, thus distorting the data signal in the time domain.

In the remainder of the paper, we will refer to "MI-crosstalk" as the sum of these two effects, induced by the DAS signal propagation on the data channel. From a system viewpoint, the impact of the first effect (optical noise enhancement) on data can be partially reduced by employing a narrow receiver optical filter (see Fig. 1 and related discussion in Section II) with variable bandwidth $B_{\mathrm{rx}}$, centered at the central frequency of the data channel. In the following, we discuss the impact of narrowing $B_{\mathrm{rx}}$.

To obtain a first-order time-domain analysis of the MI-crosstalk impact on data, we recorded the photodiode current intensity $I$ through the RTO and offline-processed it. As an example, the raw data signal intensity $I$ versus time is reported in the inset of Fig. 4a), for $P_{DAS} = 23.5$ dBm, zoomed around the DAS pulse occurrence. Notice that the long term mean value was removed. It is useful to remind here that we intentionally synchronized our system to generate one DAS pulse for each PRBS data sequence, so that the relative time-position of the pulse is time-synchronous with each PRBS sequence. In the following figures, we show the offline-processed signal $\langle I \rangle$ obtained as follows. First, we "chopped" the received $I$ over 50 time-windows, each with duration $T_{PRBS}$. Then, we evaluated the average $I$ over these recorded 50 PRBS repetitions. This averaging is fundamental to strongly reduce the impact of the underlying random noise. Figure 4 shows the evolution of $\langle I \rangle$ versus time, zooming in on a symmetric 150 ns window centered around the DAS pulse with 80 ns time duration, for different $P_{DAS}$ values. The resulting $\langle I \rangle$ waveforms (which we also AC-coupled to remove their long term mean) clearly show that, during the MI-induced interaction with the DAS pulse, the received data signal can be strongly distorted, depending on $P_{DAS}$ values. Different $P_{DAS}$, spanning from 23.5 dBm to 29.2 dBm, have been reported, while Fig. 4 refers to $\Delta f = 50$ GHz, $\Delta f = 100$ GHz and $\Delta f = 200$ GHz. The $B_{\mathrm{rx}}$ value is fixed to 14 GHz.

Interestingly, from Figs. 4a-b), two main effects are worth of attention: the impact of proximity to the DAS central frequency and the shape of the crosstalk induced on the data channel. Regarding the first one, with $\Delta f = 50$ GHz, the effect of MI starts to occur already at $P_{DAS} = 23.5$ dBm, with non-negligible distortion corresponding to 4 times the data peak-to-peak swing $I_{pp}$ (see Fig. 4a) and inset). Moreover, using (somehow extreme) high peak powers around $P_{DAS} = 28$ dBm, $\langle I \rangle$ increases approximately by 60 times the data stream $I_{pp}$, and thereby indicating a strong effect of the MI-crosstalk. For the same $P_{DAS} = 23.5$ dBm, $\Delta f = 100$ GHz in Fig. 4b) does not show any sign of distortion, which starts to be comparable with $\Delta f = 50$ GHz if employing a $P_{DAS} \sim$ 3-4 dB higher. In Fig. 4a), the case at pulse peak power $\sim$ 29 dBm was not recorded, as it could damage the PD, while it is shown in Fig. 4b). At the highest recorded $P_{DAS}$, the effect reduces by an order of magnitude when the separation is increased from 50 GHz to 100 GHz (60 a.u. for the $\Delta f = 100$ GHz case), demonstrating the effectiveness of using larger frequency spacings to decrease the amount of MI-induced crosstalk. This is made even more explicit in Fig. 4c), for the case with $\Delta f = 200$ GHz. The data waveform distortion is completely absent for $P_{DAS} <\sim 29$ dBm, and weakly appearing for higher peak powers. This is slightly noticeable in the two most right waveforms ($P_{DAS} > 28$ dBm), around 50 ns. The second physical effect concerns the imbalanced shape of the crosstalk during the pulse co-propagation (i.e., the central 80 ns of the total 150 ns), clearly visible in Figs. 4a-b). Because of the linear change of central frequency inside the pulse, due to chirp, the MI-generated spectrum, as seen in Fig. 3 for a fixed $P_{DAS}$, broadens inside the $\tau = 80$ ns, by a factor $\Delta\nu$. This leads to a time-dependent crosstalk over the data stream, which explains the clear imbalance, for both $\Delta f$ values in Figs. 4a-b), of the $\langle I \rangle$ values from the beginning to the end of the pulse co-propagation. This effect is particularly intense for high $P_{DAS} \geq 26$ dBm. For the $\Delta f = 200$ GHz case in Fig. 4c), the crosstalk is too weak to make the imbalance noticeable.

Similar observations were made in our experiments for the other filter bandwidths $B_{\text{rx}}$ and 400 GHz frequency spacing. These results are not reported here due to space limitations.

### *C. Bit Error Rate evaluation*

In order to observe the effect of the DAS pulse propagation on the data transmission performance, in this section we present the experimental BER measurements. Before proceeding, we point out that:

- the baseline BER without pulse interaction is the typical one for non-optically pre-amplified direct-detection receivers, thus mostly being limited by the Gaussian-like noise introduced by the transimpedance amplifier placed after the photodiode;
- in the presence of DAS pulse interaction, the evolution of BER in our setup will be non-stationary over time, since we clearly showed in the previous Subsection III-B that the MI-crosstalk is present only inside the DAS pulse time window. However, when present, it can be very strong, requiring the estimation of a sort of "time-resolved" BER. To do this, we resort to a similar approach employed to evaluate the $\langle I \rangle$ metric. For more information on this experimental derivation on time-resolved BER estimation, the interested reader can refer to this previous work of ours (see Fig.1(c) in [40], which anyway was related to a different transmission scenario).

We start by reporting in Fig. 5 the "instantaneous" BER ($BER_i$) for the same cases of Figs. 4a-b) ($\Delta f = 50$ GHz, 100 GHz, and $B_{\text{rx}} = 14$ GHz). The $BER_i$ time evolution has been computed considering consecutive windows of 100 bits each (i.e. 10 ns) for each of 50 PRBS periods (i.e. 5000 bits per window). We then centered the plots in Fig. 5 around the same 150 ns of Fig. 4a-b).

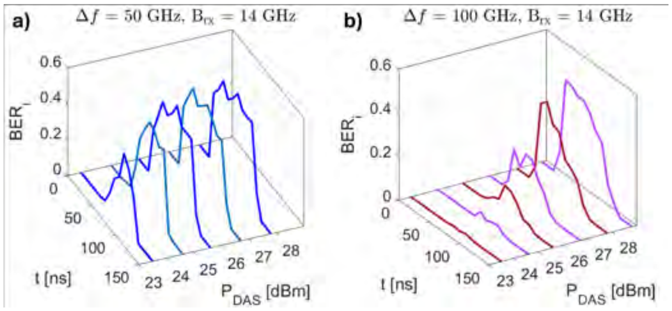

Fig. 5. Instantaneous BER time-evolution along the pulse co-propagation with data for $B_{\text{rx}} = 14$ GHz, when a) $\Delta f = 50$ GHz and b) $\Delta f = 100$ GHz, versus $P_{DAS}$. Different colors are only used to provide contrast between lines and enhance readability.

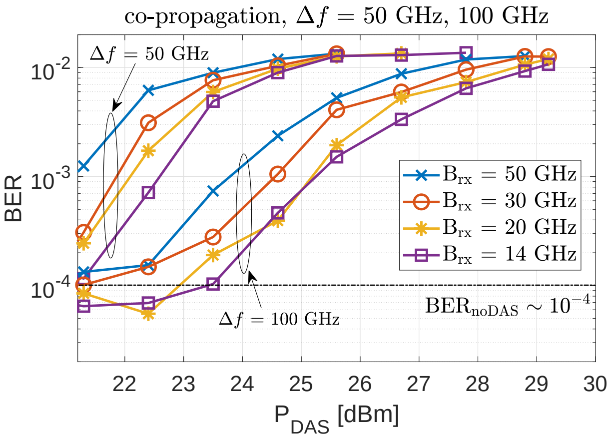

Fig. 6. BER curve versus $P_{DAS}$ values when co-propagating data and chirped pulse, for $\Delta f = 50$ GHz and $\Delta f = 100$ GHz. Four different optical filter bandwidths have been tested for both cases.

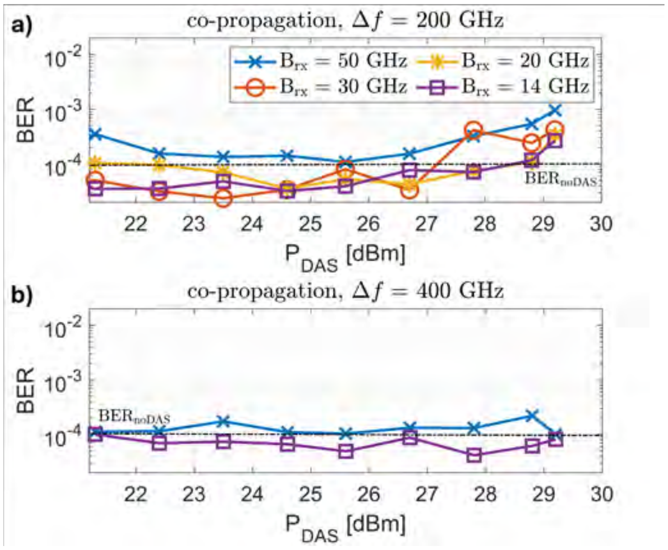

Fig. 7. BER curve versus increasing $P_{DAS}$ values when co-propagating data and chirped pulse, for a) $\Delta f = 200$ GHz and b) $\Delta f = 400$ GHz. Four different optical filter bandwidths have been tested for the former, while only two for the latter. Legend is shared between a) and b).

The results reported in Fig.5a) shows that MI can be so strong for $P_{DAS} \geq 24.6$ dBm that $BER_i$ reaches 0.5 when the DAS pulse is on, a situation that would made the data transmission to go completely out of service. The scenario significantly changes in Fig. 5b) which analyzes a larger spacing $\Delta f = 100$ GHz. A comparable effect with $\Delta f = 50$ GHz at $P_{DAS} = 24.6$ dBm can be noticed when $P_{DAS} \sim 28$ dBm, i.e. $\sim 3$ dB higher. In this case, since crosstalk is weaker (see Fig. 4b)), the $BER_i$ does not show any saturation at any of the considered peak power levels. Interestingly, the $\langle I \rangle$ shape imbalance in Fig. 4b), particularly for $P_{DAS} \geq 27$ dBm, completely reflects the $BER_i$ evolution in Fig. 5b). The broadening of the MI spectrum due to the chirp induces a higher number of errors at the rising edge of the pulse than at the falling edge, forcing a time dependency

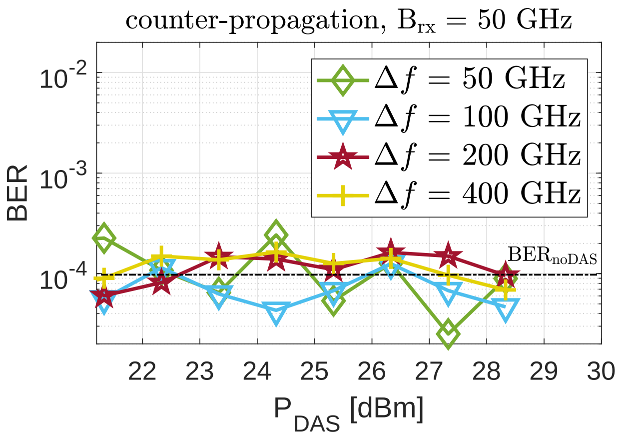

Fig. 8. BER curve versus increasing $P_{DAS}$ values when counter-propagating data and chirped pulse, for different $\Delta f$ and same optical filter bandwidth $B_{\mathrm{rx}}$.

of the BER along the 80 ns of pulse co-propagation with the data channel.

Figures 6, 7 show the BER (averaged on the full received experimental time window, equal in this case to about 200 $\mu$s, i.e. more than 60 PRBS periods), as a function of $P_{DAS}$ for different conditions of channel frequency spacing $\Delta f$ and optical filter bandwidth $B_{\mathrm{rx}}$. BER curves are shown in Fig. 6 for $\Delta f = 50$ GHz and 100 GHz, in Fig. 7a) for $\Delta f = 200$ GHz and in Fig. 7b) for $\Delta f = 400$ GHz. The black dashed line labeled $BER_{noDAS}$ represents the baseline BER value when no DAS pulse is sent into the fiber, serving as a reference point for comparison. To have a quantitative estimation of the maximum acceptable $P_{DAS}$ levels allowing co-existence, we define the following power metrics:

- $P_{th}$ is the value of $P_{DAS}$ for which the resulting BER is $\simeq BER_{noDAS}$, i.e. the power level above which the BER vs. $P_{DAS}$ curve has an inflection point;
- $P_{FECfail}$ is the $P_{DAS}$ value where the BER curve crosses $10^{-2}$, which we consider as the BER threshold before FEC.

In Fig. 6, for 100 GHz frequency separation and $B_{\mathrm{rx}} =$ 14 GHz, $P_{th} \sim 23.5$ dBm, and decreases by more than 2 dB when employing $B_{\mathrm{rx}} = 50$ GHz. The $\Delta f = 50$ GHz frequency spacing case is much more critical, as the $P_{th}$ is almost always below the considered range of $P_{DAS}$. Moreover, $P_{FECfail} \sim 27$ dBm, 3-4 dB lower than the $\Delta f = 100$ GHz case. Despite the effect of using narrower $B_{\mathrm{rx}}$ clearly shows strong improvement on the BER values (in the $\Delta f = 50$ GHz case, even one order of magnitude for $P_{DAS} = 22$ dBm when varying $B_{\mathrm{rx}}$ from 50 GHz to 14 GHz), large chirped-pulse DAS coexistence with $\Delta f = 50$ GHz spaced data channel is still quite challenging. Conversely, using increasing frequency spacings demonstrated advantages for the coexistence of the two signals, with a reduced impact of DAS pulse on the co-propagating data channel, in line with what discussed in Subsection III-A and shown in Fig. 3. In particular, Figures 7a-b) show the BER as a function of $P_{DAS}$ when the DAS and data channel are spaced by 200 GHz and 400 GHz, respectively. Despite a slight effect noticeable for $\Delta f = 200$ GHz, when using high DAS peak powers above $P_{DAS} \sim 28$ dBm, the consequences for the data channel are limited, for any of the $B_{\mathrm{rx}}$ value tested. Referring to Fig. 7b), for the $\Delta f = 400$ GHz case, there is no observable data transmission impairment for any $P_{DAS}$ tested. Figures 7a-b) confirm that coexistence with data channels spaced by 200 GHz or 400 GHz from the sensing signal can be reliably ensured. Take also into account that, when dealing with a real DAS system, the repetition period is much larger (of the order of ms), leading to a weaker effect on the average BER curves, but to an identical one in terms of instantaneous BER (see Fig. 5).

To fully address the scenario of coexistence, we also tested a counter-propagation configuration, where DAS and data signals travel in opposite directions. The rationale for trying also the counter-propagating case is related to the fact that MI is strongly dependent on phase matching conditions between the involved propagating signals, so that it is well known that MI basically disappears for the counter-propagating case [38] (just like four-wave mixing or cross-phase modulation). The used experimental setup is identical to the one presented in Fig. 1a), except for the DAS signal, which is now injected at the receiver side through the DWDM demux and propagates towards the DWDM mux. An isolator was also added at the data laser output to prevent damage. We used the same set of parameters studied for the co-propagation, such as the same $\Delta f$ values, optical filter bandwidths $B_{\mathrm{rx}}$, and the same ranges for $P_{DAS}$ values. The results with $B_{\mathrm{rx}} = 50$ GHz at all tested frequency spacings are reported in Fig. 8. The BER as a function of the $P_{DAS}$ shows no significant crosstalk induced on the data channel, with transmission performance comparable to the case when no DAS signal is present in the system at $BER_{noDAS} = 10^{-4}$. These results experimentally confirms the disappearances of any relevant nonlinear effects in this case. All the other receiver optical filter bandwidths (30 GHz, 20 GHz, 14 GHz) have also been tested with similar results to Fig. 8, but not reported due to space limitations.

To provide a summary of all the tested conditions, we summarized in Table I the main working conditions for all the different parameters. In particular, Table I shows the (approximate) values of $P_{th}$ and $P_{FECfail}$ for each $\Delta f$, $B_{\mathrm{rx}}$, and for both co-propagating and counter-propagating techniques. Considering the standard $P_{DAS} \leq 23$ dBm for DAS systems, a $\Delta f = 100$ GHz data channel would not be affected by co-propagation with the sensing signal, if using $B_{\mathrm{rx}} = 20$ GHz or 14 GHz ($P_{th} \geq 23$ dBm in these cases). Instead, a $\Delta f = 50$ GHz spacing is critical, resulting in a maximum admissible $P_{DAS} \leq 21.2$ dBm when the narrower $B_{\mathrm{rx}} = 14$ GHz filter bandwidth is used. The conditions where we experimentally verified reliable coexistence are with $\Delta f =$ 400 GHz or counter-propagation, where no consequences have been recorded on the data channel, for any $P_{DAS}$. Employing $\Delta f \geq 200$ GHz, the effect of crosstalk is so small that even larger $B_{\mathrm{rx}}$ up to 50 GHz can be employed. In this case, $P_{th}$ is usually more than 4 dB higher than 23 dBm. Table I also highlights that filtering is crucial, but a larger $\Delta f$ is more effective in reducing crosstalk. While increasing $\Delta f$ from 50 GHz to 100 GHz raises $P_{FECfail}$ by 4 dB, fixing $\Delta f$ and narrowing $B_{\mathrm{rx}}$ shows variation of $P_{FECfail}$ of 1 dB

TABLE I

$P_{th}$ AND $P_{FECfail}$ VALUES FOR CO-/COUNTER-PROPAGATING SIGNALS, CONSIDERING ALL THE TESTED $B_{\mathrm{rx}}$ AND $\Delta f$. N.C. IS SHORT FOR "NO CONSEQUENCES" RECORDED ON THE BER, FOR THOSE PARAMETERS.

| *Setup* | $\Delta f$ | $B_{\mathrm{rx}} = 14$ GHz | | $B_{\mathrm{rx}} = 20$ GHz | | $B_{\mathrm{rx}} = 30$ GHz | | $B_{\mathrm{rx}} = 50$ GHz | |
|---|---|---|---|---|---|---|---|---|---|
| | | $P_{th}$ | $P_{FECfail}$ | $P_{th}$ | $P_{FECfail}$ | $P_{th}$ | $P_{FECfail}$ | $P_{th}$ | $P_{FECfail}$ |
| **co-prop.** | 50 GHz | 21.2 dBm | 25 dBm | $<$ 21.2 dBm | 25 dBm | $<$ 21.2 dBm | 24.5 dBm | $<$ 21.2dBm | 24dBm |
| | 100 GHz | 23.5 dBm | 29 dBm | 23 dBm | 28.8 dBm | 21.2 dBm | 28 dBm | $<$ 21 dBm | 27 dBm |
| | 200 GHz | 28.8 dBm | $>$ 29.2 dBm | 28.8 dBm | $>$ 29.2 dBm | 27 dBm | $>$ 29.2 dBm | 27 dBm | $>$ 29.2 dBm |
| | 400 GHz | N.C. | N.C. | N.C. | N.C. | N.C. | N.C. | N.C. | N.C. |
| **counter-pr.** | N.C. | | | | | | | | |

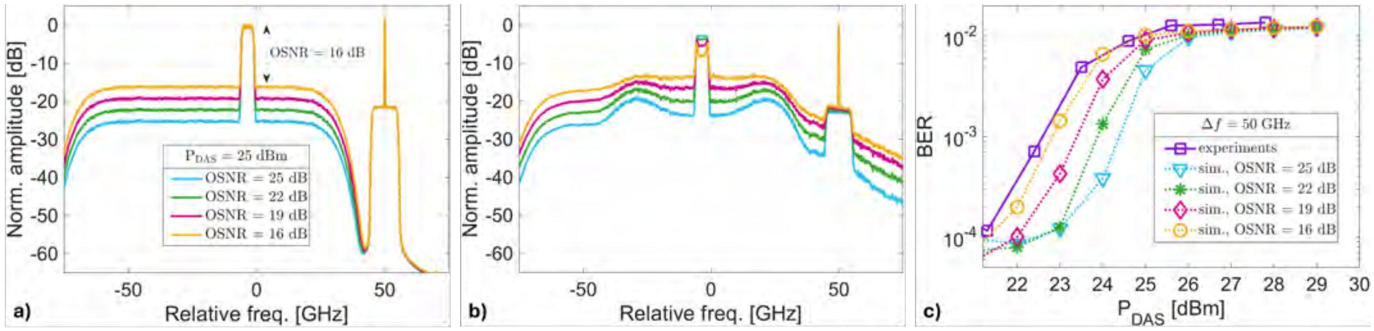

Fig. 9. Spectra of transmitted DAS pulse + data a) before and b) after fiber propagation with $\Delta f = 50$ GHz data channel, when considering different OSNR values, for $P_{DAS} = 25$ dBm. All spectra have been normalized to the maximum value when transmitting $P_{DAS} = 25$ dBm. Graph c) shows the BER as a function of the $P_{DAS}$ for both experiments and numerical simulations for different OSNR values.

for 50 GHz spacing and 2 dB for 100 GHz spacing. This happens because the crosstalk distortion on the data channel at $P_{FECfail}$ is at its highest point, and the filter's effectiveness limited.

## IV. NUMERICAL SIMULATIONS

The scenarios outlined in the previous section for the co-propagation experiment have also been examined through detailed time-domain split-step numerical simulations. These simulations not only confirm the results obtained but also provide deeper insights into the key nonlinear interactions between the DAS signal, the data signal, and noise. Furthermore, they allow for the exploration of a broader range of parameters, including the investigation of additional optical filtering options.

We numerically simulated the same DAS pulse used in the experiments, with identical intensity shape, chirp content, duration, and the same range of peak powers. In particular, ten DAS pulses are generated along the 10 Gbit/s data stream, thus the total simulated time window is equal to $\sim 32$ $\mu$s, again with 2.4% duty cycle. The shorter simulation window compared to the experiments was a compromise between CPU computational time and accuracy, and, as we will show later, still allows us to obtain results that can be compared to the experiments (i.e., the same BER saturation level and similar average spectra). The fiber length considered for the simulations is again 10 km, and only the optimal $B_{\mathrm{rx}} = 14$ GHz optical filter bandwidth was tested. Flat noise from the transimpedance amplifier (TIA) was added to the received signal, and its power spectral density was adjusted to have the same sensitivity curve for $BER_{noDAS}$ as in the experiments. As detailed in Section II when discussing Fig. 1b), the two extra optical noise contributions coming from the DAS transmitter branch are the *I/Q modulator harmonics* and the *ASE noise* (generated by the EDFA used in the DAS trasmitter). As shown in Fig. 2a), MI intensifies this optical noise, with the resulting main lobes frequency position depending on the pulse peak power according to Eq. (1). While ASE noise can be easily added in simulations, the peculiar shape of the harmonics in Fig. 1b) is more complex to be emulated in simulation. The harmonics are specific to our experimental setup, thus, in our numerical simulations, we decided to neglect them. Instead, we focused on testing various levels of ASE noise. This approach allowed us to intentionally generate a wider range of transmitted-side OSNRs than the one present in our setup. By doing this, we aimed to gain a clearer understanding of the general impact of optical noise levels, which are subsequently influenced by the nonlinear effects in the optical link. In particular, in our simulation, ASE noise is generated as usual as a flat complex white Gaussian noise and it is then passed through a Super-Gaussian filter of nominal bandwidth $B_{\mathrm{tx}} = 100$ GHz. We chose this value for the flat ASE noise to reasonably fit the overall experimental noise sources bandwidth (80 GHz flat ASE noise + I/Q modulator harmonics, resulting in a total $\sim$ 95 GHz wide bandwidth, see Fig. 1b)). Moreover, the filtered ASE noise was positioned around the DAS pulse to match the experiments. The resulting transmitted spectra are reported in Fig. 9a) for 50 GHz frequency spaced data channels. Here, $P_{DAS} = 25$ dBm, while the ASE noise level was tweaked to have different OSNRs of 25 dB, 22 dB,

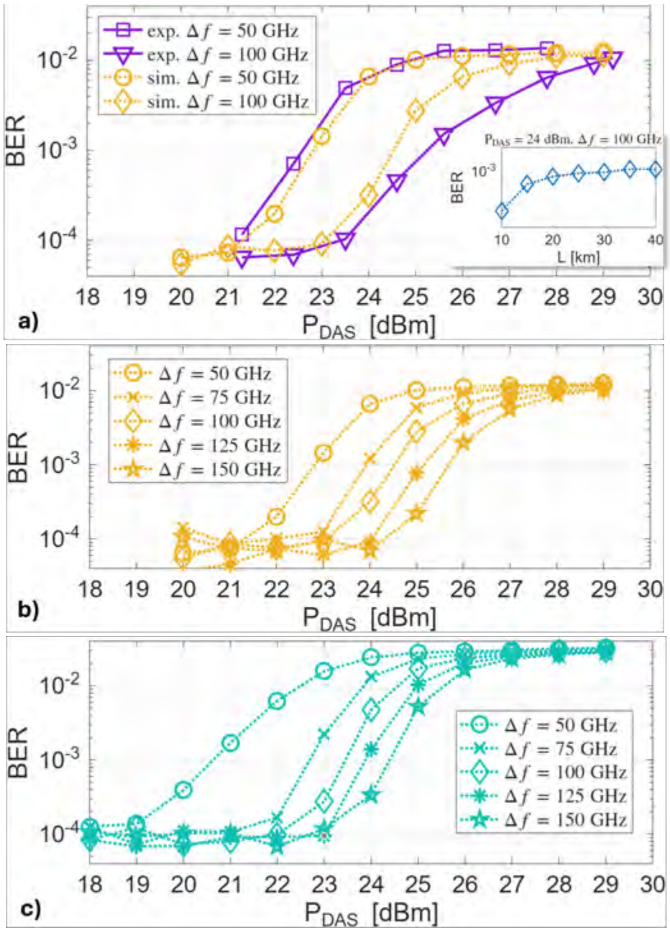

Fig. 10. BER curves versus $P_{DAS}$ for a) $\Delta f = 50$ GHz and 100 GHz with $B_{\mathrm{rx}} = 14$ GHz for both experiments, and simulations. Inset shows the simulated BER versus fiber length, when $P_{DAS} = 24$ dBm and $\Delta f = 100$ GHz. Simulation-only BER curves for increasing $\Delta f$ values from 50 GHz to 150 GHz in steps of 25 GHz are shown in b) for the PAM-2 and c) for the PAM-4 modulation formats. All the simulations have been obtained setting OSNR = 16 dB.

19 dB, and 16 dB. We then propagated the signals in Fig. 9a) and recorded the received spectra in Fig. 9b) at the fiber output. In both Figs. 9a-b) all spectra are normalized to the maximum of the DAS pulse transmitted spectrum, so that Fig. 9a) shows the DAS pulse spectra maxima at 0 dB. Notice that the received spectra depict the two MI lobes on either side of $f_{DAS}$, such as those predicted by the theory in Fig. 2a). Figures 9a-b) confirm our earlier observations. Although optical noise is minimal on the data channel due to the transmitter side optical filtering, it increases after fiber propagation because of strong MI caused by high-peak-power DAS pulses. Specifically, Figure 9b) illustrates that, as the OSNR decreases, the MI-induced optical noise around the data channel rises significantly.

We also analyzed the BER performance in simulation, as shown in Figure 9c). This figure illustrates the BER evolution versus $P_{DAS}$ for a frequency separation of $\Delta f = 50$ GHz, incorporating various OSNR values varied in 3 dB increments: for OSNR= 25 dB the BER starts to rise at $P_{DAS} \sim 23$ dBm, 2 dB higher than the case for OSNR = 16 dB. In other words, the effect of MI on the data channel is triggered for lower $P_{DAS}$ values if the OSNR is decreased. These results lead to a possible design rule: the lower the optical noise generated by the DAS transmitter setup, the higher $P_{DAS}$ can be allowed. We also point out that the curve for OSNR=16 dB matches our experimental BER curve, where the same 16 dB OSNR was observed between the DAS pulse and the highest I/Q modulator harmonic (see Fig. 1b)). In the reminder of the paper, we will show results for OSNR=16 dB only. The BER curves for experiments and simulations when $\Delta f = 50$ GHz, 100 GHz, and $B_{\mathrm{rx}} = 14$ GHz are shown in Fig. 10a). The agreement with experiments is very good in the 50 GHz case, whereas small discrepancies can be observed in the 100 GHz case for $P_{DAS} \geq 25$ dBm. This can be attributed to a non-perfect reproduction of the shape of the noise in the numerical simulations. A flat ASE noise (such as the one we have in simulation) amplified by the MI could generate a flatter spectrum for increasing $P_{DAS}$. This leads to an almost perfect match between experimental and simulation BER when $P_{DAS} < 24.6$ dBm, but to a mismatch at higher peak power, as if the tails of the MI-amplified noise spectrum were still intense. Overall, the reasonable match of the experimental and numerical simulation BER curves with OSNR = 16 dB means that the MI crosstalk on the data channel can be reliably predicted.

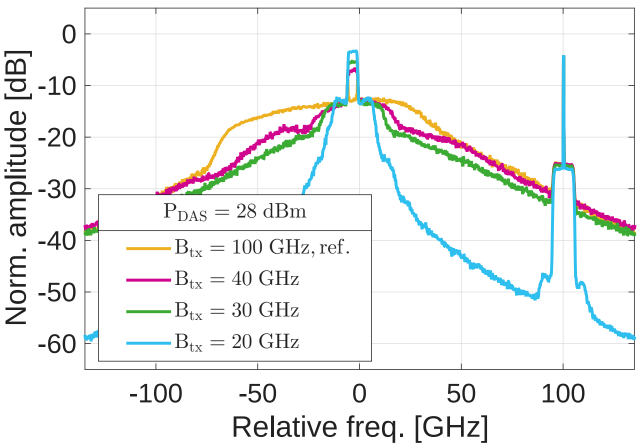

Fig. 11. Spectra of the received DAS + 100 GHz spaced data channel when considering $P_{DAS} = 28$ dBm and varying $B_{\mathrm{tx}}$. The yellow curve refers to the reference case with 100 GHz wide noise bandwidth employed to emulate the DWDM.

The inset of Figure 10a) shows the BER evolution versus fiber length $L$, assuming $P_{DAS} = 24$ dBm, $\Delta f = 100$ GHz and the same OSNR and $B_{\mathrm{rx}}$ of the main figure, obtained through simulations. As expected, the effect of MI-crosstalk on the data effect saturates around $L \sim 25$ km, which is the usual fiber length where the effect of nonlinearities is stronger. For lengths $L \geq 25$ km, the recorded BER values remain one order of magnitude lower compared to those recorded under worse conditions (higher $P_{DAS}$, wider $B_{\mathrm{rx}}$, lower $\Delta f$) at $L = 10$ km, which saturates at $10^{-2}$. Figure 10b) shows the BER curves varying $\Delta f$ from 50 GHz to 150 GHz in steps of 25 GHz. These simulation results further confirm the importance of using larger frequency spacings, as the BER

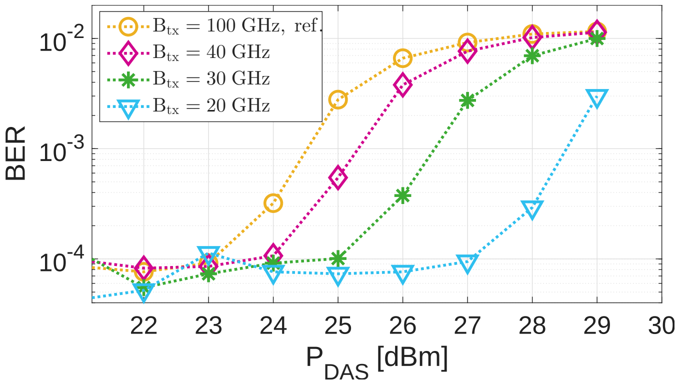

Fig. 12. BER curves versus $P_{DAS}$ obtained in numerical simulations, when employing narrower optical filter bandwidths $B_{\mathrm{tx}}$ at the transmitter side, around the DAS channel. The yellow curve refers to the reference 100 GHz wide noise bandwidth employed to emulate the experimental DWDM.

shows increasing tolerance to the DAS peak power for increasing $\Delta f$. This results in more than 3 dB higher admissible $P_{DAS}$ when $\Delta f$ is increased from 50 GHz to 150 GHz, at BER $= 10^{-4}$. To provide a more comprehensive scenario we also ran, just for this specific case, numerical simulations changing the modulation format to PAM-4, spanning the same $\Delta f$ range of Fig. 10b). The average BER versus $P_{DAS}$ curves are reported in Fig. 10c). The DAS peak powers range has been increased to include 18 dBm and 19 dBm, to show where the effect of DAS is negligible for this modulation format. As expected, the penalty on the PAM-4, introduced by the co-propagating sensing signal, is higher than the PAM-2 case. Particularly, the MI-induced crosstalk starts to have consequences on the PAM-4 average BER for $P_{DAS}$ values 1-2 dB lower than the PAM-2 modulation format analyzed until now. Additionally, the BER curves for the PAM-4 saturates at a slightly higher BER value than the PAM-2 case.

As shown in Table I, a proper optical filtering at the receiver can help reduce the amount of noise and limit the onset of MI, thus reducing the generated crosstalk on the data channel. We also investigate the possibility of introducing filtering on the DAS signal to restrict the noise bandwidth at the transmitter side. In Fig. 9, the Super-Gaussian shape of the filter has bandwidth $B_{\mathrm{tx}} = 100$ GHz, and it is not centered around the chirped signal because we wanted to emulate, as closely as possible, the experimental scenario. To try to improve the performance, we made further investigations, centering the filter around the DAS pulse and testing narrower bandwidths $B_{\mathrm{tx}}$: 40 GHz, 30 GHz and 20 GHz. Fig. 11 shows the resulting spectra after fiber propagation, when co-propagating with a $\Delta f = 100$ GHz-spaced data channel and employing $P_{DAS} = 28$ dBm. Spectra are normalized with respect to the related transmitted spectrum maximum of the DAS pulse (as was done for Figs. 9a-b)). The difference, in terms of crosstalk, is small between $B_{\mathrm{tx}} = 40$ GHz and the reference $B_{\mathrm{tx}} = 100$ GHz case, and slightly enhanced when further decreasing the bandwidth to $B_{\mathrm{tx}} = 30$ GHz. A significant difference is instead present when employing $B_{\mathrm{tx}} = 20$ GHz, which is likely shaping the noise to a too small bandwidth for the main lobes of the MI gain to properly amplify it. The related BER curves for the different conditions analyzed in Fig. 11 are shown in Fig. 12, reporting an important enhancement of the BER for decreasing $B_{\mathrm{tx}}$.

## V. FINAL DISCUSSIONS AND CONCLUSIONS

This paper discusses in detail the coexistence of large chirped-pulse DAS and IM-DD systems on the same fiber, primarily focusing on the impact on data channels. Our findings identified Kerr-related MI, caused by propagation of high-peak-power pulses from DAS, as the main impairment affecting data transmission. We investigated the impact of the variation of numerous parameters, which enabled us to summarize the following "system guidelines" for designing future fiber links where the coexistence of DAS and data transmission is necessary.

- **Counter-propagation.** The experimental setup in which the DAS pulse is transmitted in the opposite direction with respect to the data shows negligible nonlinear effects on the data channels. Thus, when possible from a network architecture viewpoint, this should be the preferred option.
- **Co-propagation.** When, on the contrary, co-propagation is a must from an architectural viewpoint, the signals' coexistence has been demonstrated both experimentally and through numerical simulations, but only after a careful selection of the main transmission parameters. Given that the MI-induced crosstalk is the main impairment on data, the 50 GHz spacing should be avoided (unless DAS peak power can be kept very low, such as below 20 dBm), while 100 GHz spacing allows DAS peak power up to $\sim$ 23 dBm, a value that is compliant with the one often used in commercial DAS systems. If 150 GHz or 200 GHz (or higher, such as 400 GHz) spacing is acceptable from an architectural viewpoint, then this is the preferred system option, allowing DAS peak power above 28 dBm with negligible impact on data. These conclusions on large spectral spacing would become even more relevant for a longer fiber link (we addressed 10 km in this paper) or for multi-span optically amplified scenarios where one DAS is inserted in each span (just like what is done today for the optical supervisory channel, OSC).
- **Transmitter and receiver filters, in co-propagation**. The transmitted side noise, if possible, should be kept as low as possible, as MI intensifies it. Narrow optical filtering on the transmitter side, around the DAS pulse, has also been shown to limit the MI onset. Similarly, strong optical filtering on the receiver side, around the data channel, reduces the amount of MI-crosstalk, improving the coexistence of the two signals.

Even though it is not addressed in this paper, we point out that a possible strategy for co-propagation would be to position the DAS signal completely off-band, i.e., several nanometers away from the data wavelengths. The only limitation of this approach would be the onset of Raman nonlinearity, which reaches its maximum when the "pump and probe" signals are about 12 THz apart. These consideration are outside the scope of this paper, but may lead to an interesting future research work.

In our further studies, we also plan to address the coexistence of DAS with Polarization Multiplexed-Quadrature Amplitude Modulation (PM-QAM) coherent telecommunication systems [41]. In this scenario, the impact on data would be more complex, since coherent detection is also phase-sensitive. In addition to MI, cross-phase modulation nonlinearity may also become relevant.

## REFERENCES

[1] J. S. Wey, "Distributed Fiber Optic Sensing (DFOS) in Telecom Networks: Industry Trends and Standards Development," *IEEE/OPTICA Journal of Lightwave Technology*, pp. 1–7, 2025.

[2] S. Pellegrini, L. Minelli, L. Andrenacci, G. Rizzelli, D. Pilori, G. Bosco, L. D. Chiesa, C. Crognale, S. Piciaccia, and R. Gaudino, "Overview on the state of polarization sensing: application scenarios and anomaly detection algorithms," *IEEE/OPTICA J. Opt. Commun. Netw.*, vol. 17, pp. A196–A209, 02 2025.

[3] L. Andrenacci, D. Pilori, S. Pellegrini, L. Minelli, G. Bosco, C. Crognale, S. Piciaccia, and R. Gaudino, "Comparison between Phase and Polarization Sensing using Coherent Transceivers over Deployed Metro Fibers," in *2024 Optical Fiber Communications Conference and Exhibition (OFC)*, pp. 1–3, 2024.

[4] A. Mecozzi, "Sensing with submarine optical cables," *APL Photonics*, vol. 9, p. 070902, 07 2024.

[5] I. D. Luch, P. Boffi, M. Ferrario, G. Rizzelli, R. Gaudino, and M. Martinelli, "Vibration Sensing for Deployed Metropolitan Fiber Infrastructure," *IEEE/OSA Journal of Lightwave Technology*, vol. 39, no. 4, pp. 1204–1211, 2021.

[6] S. J. Savory, "Digital Coherent Optical Receivers: Algorithms and Subsystems," *IEEE Journal of Selected Topics in Quantum Electronics*, vol. 16, no. 5, pp. 1164–1179, 2010.

[7] A. Mecozzi, C. Antonelli, M. Mazur, N. Fontaine, H. Chen, L. Dallachiesa, and R. Ryf, "Use of Optical Coherent Detection for Environmental Sensing," *IEEE/OPTICA Journal of Lightwave Technology*, vol. 41, no. 11, pp. 3350–3357, 2023.

[8] L. Costa, S. Varughese, P. Mertz, V. Kamalov, and Z. Zhan, "Localization of seismic waves with submarine fiber optics using polarization-only measurements," *Communications Engineering*, vol. 2, p. 070902, 12 2023.

[9] E. Ip, Y.-K. Huang, G. Wellbrock, T. Xia, M.-F. Huang, T. Wang, and Y. Aono, "Vibration Detection and Localization Using Modified Digital Coherent Telecom Transponders," *IEEE/OPTICA J. Lightwave Technol.*, vol. 40, pp. 1472–1482, Mar 2022.

[10] A. Hartog, *An Introduction to Distributed Optical Fibre Sensors*. CRC Press, first edition ed., 2017.

[11] L. B. Liokumovich, N. A. Ushakov, O. I. Kotov, M. A. Bisyarin, and A. H. Hartog, "Fundamentals of Optical Fiber Sensing Schemes Based on Coherent Optical Time Domain Reflectometry: Signal Model Under Static Fiber Conditions," *IEEE/OSA Journal of Lightwave Technology*, vol. 33, no. 17, pp. 3660–3671, 2015.

[12] E. F. Williams, M. R. Fernández-Ruiz, R. Magalhaes, R. Vanthillo, Z. Zhan, M. González-Herráez, and H. F. Martins, "Distributed sensing of microseisms and teleseisms with submarine dark fibers," *Nature Communications*, vol. 10, 2019.

[13] J. Liu, S. Yuan, Y. Dong, B. Biondi, and H. Y. Noh, "TelecomTM: A Fine-Grained and Ubiquitous Traffic Monitoring System Using Pre-Existing Telecommunication Fiber-Optic Cables as Sensors," *Proc. ACM Interact. Mob. Wearable Ubiquitous Technol.*, vol. 7, 06 2023.

[14] E. Biondi, J. Li, E. Bird, and Z. Zhan, "Subsurface Monitoring and Imaging Based on DAS," in *Optical Fiber Communication Conference (OFC) 2025*, p. W3G.1, Optica Publishing Group, 2025.

[15] E. Piñeiro, M. Sagues, and A. Loayssa, "Compensation of phase noise impairments in distributed acoustic sensors based on optical pulse compression time-domain reflectometry," *Journal of Lightwave Technology*, vol. 41, no. 10, pp. 3199–3207, 2023.

[16] D. Chen, Q. Liu, and Z. He, "108-km Distributed Acoustic Sensor With 220-p$\varepsilon/\sqrt{\mathrm{Hz}}$ Strain Resolution and 5-m Spatial Resolution," *Journal of Lightwave Technology*, vol. 37, no. 18, pp. 4462–4468, 2019.

[17] O. H. Waagaard, E. Rønnekleiv, A. Haukanes, F. Stabo-Eeg, D. Thingbø, S. Forbord, S. E. Aasen, and J. K. Brenne, "Real-time low noise distributed acoustic sensing in 171 km low loss fiber," *OSA Continuum*, vol. 4, pp. 688–701, Feb 2021.

[18] H. F. Martins, K. Shi, B. C. Thomsen, S. Martin-Lopez, M. Gonzalez-Herraez, and S. J. Savory, "Real time dynamic strain monitoring of optical links using the backreflection of live PSK data," *Opt. Express*, vol. 24, pp. 22303–22318, Sep 2016.

[19] D. Chen, Q. Liu, and Z. He, "High-fidelity distributed fiber-optic acoustic sensor with fading noise suppressed and sub-meter spatial resolution," *Opt. Express*, vol. 26, pp. 16138–16146, Jun 2018.

[20] E. Ip, Y.-K. Huang, M.-F. Huang, F. Yaman, G. Wellbrock, T. Xia, T. Wang, K. Asahi, and Y. Aono, "DAS Over 1,007-km Hybrid Link With 10-Tb/s DP-16QAM Co-Propagation Using Frequency-Diverse Chirped Pulses," *IEEE/OPTICA J. Lightw. Technol.*, vol. 41, pp. 1077–1086, 2023.

[21] E. Rønnekleiv, T. Sørgård, D. Klimentov, N. Tolstik, O. H. Waagaard, J. Jacobsen, F. Stabo-Eeg, O. A. Sab, A. Calsat, P. Plantady, and J. K. Brenne, "Range-scalable distributed acoustic sensing with EDFA repeaters demonstrated over 2227 km," *Opt. Lett.*, vol. 50, pp. 25–28, Jan 2025.

[22] J. Pastor-Graells, H. F. Martins, A. Garcia-Ruiz, S. Martin-Lopez, and M. Gonzalez-Herraez, "Single-shot distributed temperature and strain tracking using direct detection phase-sensitive OTDR with chirped pulses," *Opt. Express*, vol. 24, pp. 13121–13133, 06 2016.

[23] H. D. Bhatta, L. Costa, A. Garcia-Ruiz, M. R. Fernandez-Ruiz, H. F. Martins, M. Tur, and M. Gonzalez-Herraez, "Dynamic Measurements of 1000 Microstrains Using Chirped-Pulse Phase-Sensitive Optical Time-Domain Reflectometry," *Journal of Lightwave Technology*, vol. 37, no. 18, pp. 4888–4895, 2019.

[24] H. F. Martins, "Large chirped-pulse phi-OTDR for single-shot to day-long nano-strain measurements with high dynamic range," in *29th International Conference on Optical Fiber Sensors* (J. L. Santos, M. L.-A. Sainz, and T. Sun, eds.), vol. 13639, p. 136392R, International Society for Optics and Photonics, SPIE, 2025.

[25] P. J. Vidal-Moreno, E. Rochat, P. Fermoso, M. R. Fernández-Ruiz, H. Martins, S. Martin-Lopez, M. O. na, and M. Gonzalez-Herraez, "Cancellation of reference update-induced 1/f noise in a chirped-pulse DAS," *Opt. Lett.*, vol. 47, pp. 3588–3591, Jul 2022.

[26] R. Magalhães, T. Neves, L. Scherino, S. Martin-Lopez, and H. F. Martins, "Reaching Long-Term Stability in CP-$\phi$OTDR," *Journal of Lightwave Technology*, vol. 40, no. 12, pp. 3916–3922, 2022.

[27] L. Hernández-Martín, J. Preciado-Garbayo, J. Canudo, J. D. Ania-Castañón, and H. F. Martins, "Raman-assisted large chirped-pulse phi-OTDR for long range millikelvin distributed fibre thermometry," in *29th International Conference on Optical Fiber Sensors* (J. L. Santos, M. L.-A. Sainz, and T. Sun, eds.), vol. 13639, p. 136392Q, International Society for Optics and Photonics, SPIE, 2025.

[28] M. R. Fernández-Ruiz, L. Costa, and H. F. Martins, "Distributed Acoustic Sensing Using Chirped-Pulse Phase-Sensitive OTDR Technology," *Sensors*, vol. 19, no. 20, 2019.

[29] M. R. Fernández-Ruiz, J. Pastor-Graells, H. F. Martins, A. Garcia-Ruiz, S. Martin-Lopez, and M. Gonzalez-Herraez, "Laser Phase-Noise Cancellation in Chirped-Pulse Distributed Acoustic Sensors," *Journal of Lightwave Technology*, vol. 36, no. 4, pp. 979–985, 2018.

[30] J. K. Brenne, A. Sladen, P. Pecci, J. P. Morten, J. Pelaez, J. Jacobsen, A. Calsat, P. Plantady, J.-P. Ampuero, D. Rivet, and H. Février, "Non-Intrusive DAS Coexisting in Telecom Networks," in *Optical Fiber Communication Conference (OFC) 2024*, p. M4E.3, Optica Publishing Group, 2024.

[31] Z. Jia, L. A. Campos, M. Xu, H. Zhang, M. Gonzalez-Herraez, H. F. Martins, and Z. Zhan, "Experimental Coexistence Investigation of Distributed Acoustic Sensing and Coherent Communication Systems," in *Optical Fiber Communications Conf. and Exhibition (OFC)*, 2021.

[32] H. F. Martins, S. Martin-Lopez, P. Corredera, P. Salgado, O. F. ao, and M. González-Herráez, "Modulation instability-induced fading in phase-sensitive optical time-domain reflectometry," *Opt. Lett.*, vol. 38, pp. 872–874, 03 2013.

[33] J. S. Wey, "Accelerating Distributed Fiber Optic Sensing (DFOS) Ecosystem Development in Metro and Access Networks," in *2025 Optical Fiber Communications Conference and Exhibition (OFC)*, pp. 1–3, 2025.

[34] S. Pellegrini, L. Hernandez-Martin, A. M. R. Brusin, G. Rizzelli, J. D. Ania-Castañon, G. Bosco, R. Gaudino, and H. F. Martins, "On the Coexistence of DAS and IMDD Systems on the Same Fiber," in *2025 25th Anniversary International Conference on Transparent Optical Networks (ICTON)*, pp. 1–4, 2025.

[35] G. Rizzelli, M. Fasano, M. Casasco, A. Madaschi, A. M. R. Brusin, P. Parolari, R. Gaudino, and P. Boffi, "Field-Trial of Real-Time Pulse-Based DAS and 400G Coherent DWDM Coexistence," in *2025 Optical Fiber Communications Conference and Exhibition (OFC)*, pp. 1–3, 2025.

[36] M. R. Fernández-Ruiz, H. F. Martins, J. Pastor-Graells, S. Martin-Lopez, and M. Gonzalez-Herraez, “Phase-sensitive OTDR probe pulse shapes robust against modulation-instability fading,” *Opt. Lett.*, vol. 41, pp. 5756–5759, Dec 2016.

[37] M. R. Fernández-Ruiz, H. F. Martins, L. Costa, S. Martin-Lopez, and M. Gonzalez-Herraez, “Steady-Sensitivity Distributed Acoustic Sensors,” *Journal of Lightwave Technology*, vol. 36, no. 23, pp. 5690–5696, 2018.

[38] G. P. Agrawal, “Chapter 5 - optical solitons,” in *Nonlinear Fiber Optics (Fifth Edition)* (G. Agrawal, ed.), Optics and Photonics, pp. 129–191, Boston: Academic Press, fifth edition ed., 2013.

[39] M. Alem, M. A. Soto, and L. Thévenaz, “Analytical model and experimental verification of the critical power for modulation instability in optical fibers,” *Opt. Express*, vol. 23, pp. 29514–29532, 11 2015.

[40] P. Torres-Ferrera, V. Milite, V. Ferrero, M. Valvo, R. Mercinelli, and R. Gaudino, “Burst-Mode Equalization Strategies in 25 Gbps US-PON using Duobinary and 10G-Class APD for 20-km in C-Band,” in *2019 Optical Fiber Communications Conference and Exhibition (OFC)*, pp. 1–3, 2019.

[41] A. M. R. Brusin, G. Rizzelli, M. Fasano, J. Morosi, S. Pellegrini, V. Ferrero, G. Bosco, D. Pilori, P. Parolari, A. Madaschi, M. Brunero, P. Boffi, and R. Gaudino, “Overview and analysis of optical sensing techniques over deployed telecom networks,” in *2024 24th International Conference on Transparent Optical Networks (ICTON)*, pp. 1–4, 2024.